JOURNAL OF SPACECRAFT AND ROCKETS
Vol. 38, No. 4, July–August 2001

Investigation of Hypersonic Compression Ramp Heating at High Angles of Attack

Koichi Hozumi,* Yukimitsu Yamamoto,* and Keisuke Fujii*
National Aerospace Laboratory, Chofu, Tokyo 182-8522, Japan
Jean-Paul Ledy† and Dominique Devezeaux‡
ONERA, F-92322 Chatillon Cedex, France
and
Joëlle Fontaine§
ONERA, F-73500 Modane, France

To clarify the relationship of the flow structure and the heating characteristics of blunt-nose flat plates with a compression ramp, an experimental and analytical study of the hypersonic aerodynamic heating characteristics at high angles of attack has been conducted. The effect of nose bluntness and angle of attack on the heating pattern of the compression ramp has been explored, and the relationship between the ramp heating and the shock/shock interaction of the bow, separation, and compression corner shocks were examined. Triple-shock interaction plays an important role in determining the state of the flow downstream of the bow/separation shock interaction point and the resulting ramp heat transfer distribution. The interaction around the ramp may be identified as variations of an Edney type I, V, or VI interaction (Edney, B., "Anomalous Heat Transfer and Pressure Distributions on Blunt Bodies at Hypersonic Speeds in the Presence of an Impinging Shock," Aeronautical Research Inst. of Sweden, FFA Rept. 115, Stockholm, Feb. 1968). Numerical simulation of the interacting flowfield using two-dimensional laminar calculations showed discrepancy with an experimental heat transfer distribution for cases of large blunt-nose flat plates at high angles of attack. Exploratory studies of two-dimensional and three-dimensional calculations were conducted for fully laminar, fully turbulent, and transitional flow conditions to examine the reason for this discrepancy. The three-dimensional calculation showed satisfactory agreement with the experimental shock shape and separation length.

Nomenclature

AR	=	model aspect ratio, w/xc
C	=	width of the used flat plate models
C_p	=	specific heat capacity at constant pressure
d	=	leading-edge diameter
h	=	heat transfer coefficient, $q/(T_0 - T_w)$
M	=	Mach number
p	=	pressure
q	=	heat transfer rate
Re	=	Reynolds number
r_n	=	leading-edge radius
St	=	Stanton number, $h/\rho u c_p$
T	=	temperature
x	=	distance from leading edge along upstream plate direction
α	=	thermal diffusivity, angle of attack
θ	=	flow deflection angle
λ	=	thermal conductivity
ρ	=	density

Subscripts

w	=	wall condition
0	=	stagnation condition
∞	=	freestream value

Superscript

$*$	=	at Eckert's reference temperature

Introduction

THE understanding of the flow phenomena around the compression corner with a flow separation upstream from the ramp and relating a multiple shock wave interaction is significantly important for the aerothermal design of a winged reentry vehicle. The separated flow over the compression corner with an interacting shock wave has a large influence on the effectiveness of the control flap and the local and peak heating rates on the control surface. Peak heating must be predicted accurately to preserve the thermal and structural integrity of the vehicle.

Much work has been performed both experimentally and computationally to gain an accurate capability to describe the physics of flow around compression corners. The basic phenomena and the main flow features of such configurations are now well known. However, most of the work are for cases with a zero angle of attack[1–3] and only a few basic experiments for cases with higher angles of attack[4–6] have been conducted. The data at higher angles of attack are essential to evaluate the aerothermal characteristics of the control surface in a typical reentry flight regime. Evaluation of the loads in cases that follow laminar–turbulent transition induced by the interaction process is also necessary for spacecraft programs such as HOPE-X (H-II Rocket Orbiting Plane Experimental) now being developed in Japan.

In Ref. 6, a numerical study of inviscid shock interaction on double-wedge geometries was conducted at high angles of attack. Although the computed inviscid interacting flow structure was different from the actual viscous flow structure, the study shows that it is important to investigate these interacting flows to understand the heating characteristics around the compression ramp.

In the present study, for blunt-nose flat plates with a compression ramp, an experimental and analytical study of the hypersonic aerodynamic heating characteristics at a high angle of attack has been conducted using data obtained in the National Aerospace Laboratory

Presented as Paper 2000-2597 at Fluids 2000, Denver, CO, 19–22 June 2000; received 14 July 2000; revision received 2 January 2001; accepted for publication 3 January 2001. Copyright © 2001 by the American Institute of Aeronautics and Astronautics, Inc. All rights reserved.

*Research Scientist, Fluid Science Research Center, 7-44-1 Jindaiji Higashicho. Member AIAA.
†Head, Testing Division, Computing, Engineering and Testing Facilities; currently retired.
‡Representative, Launchers and Re-Entry Vehicles, Prospect and Synthesis Department.
§Test Engineer, Method Department, Experimental Group.

(NAL) 1.27-m and the ONERA S4MA hypersonic wind tunnels. The effects of nose bluntness and angle of attack on the ramp heating pattern has been explored by examining the relation between the ramp heating characteristics and the shock/shock interaction by bow, separation, and compression corner shocks. Numerical computations have also been performed and compared to the present experimental data to evaluate the numerical rebuilding capability.

Experimental Setup

Wind Tunnels

Tests were conducted in the NAL 1.27-m and the ONERA S4MA hypersonic wind tunnels at a nominal Mach number of 10 at angles of attack of 0, 15, 20, 30, and 35 deg. All tests were conducted at normally laminar-flow conditions at Reynolds numbers between 0.75×10^6/m and 1.8×10^6/m. The test cases are shown in Table 1.

The NAL 1.27-m and the ONERA S4MA hypersonic tunnels are similar Mach 10 blowdown-type tunnels with nozzle exit diameters of 1.27 and 1.0 m, respectively. A more detailed description of the tunnels may be found in Refs. 4 and 7.

Models

The same models were used in both tunnels in the present studies to compare and to evaluate heat transfer measurement techniques, especially for infrared (IR) thermography. The models consist of the central plates and a holder to support and protect them (Fig. 1). The central plates are made from a high-temperature resisting and low thermal diffusivity engineering plastic (Vespel®) whose properties are shown in Table 2. Four interchangeable leading-edge parts with different nose bluntneses ($r_n = 0.3$, 3, 6, and 12 mm) were made to obtain data on the effects of nose bluntness. A fixed compression corner angle of 15 deg was used.

Table 1 Test cases in ONERA/NAL test campaigns

NAL run no.	ONERA run no.	Model	p_0, bar	T_0, K	α, deg
616	2915	B	25	1100	0
624	——	B	25	1100	15
336	2917	B	25	1100	20
340	2918	B	25	1100	30
622	——	B	25	1100	30
619	2919	B	25	1100	35
614	——	D	60	1100	0
613	——	D	25	1100	0
334	2923	D	25	1100	20
623	2921	D	25	1100	30
621	2920	D	25	1100	35
615	(1048)	C	25	1100	0
339	2924	C	25	1100	30
620	2925	C	25	1100	35
617	(1045)	A	25	1100	0
341	2927	A	25	1100	30
618	2926	A	25	1100	35
	Additional test cases				
Roughness test					
324[a]	——	A	25	1100	30
337	——	A	25	1100	20
346[a]	——	A	25	1100	20
Oil flow test					
1068	——	D	25	1100	35
1069	——	A	25	1100	35

[a]With carborundum roughness band, height 0.3 mm, width 5 mm, and location 1 mm from leading edge.

Table 2 Thermal properties of Vespel

	T, °C					
Parameter	25	50	100	150	200	300
$C_p \times 10^3$, J/kgK	1.01	1.10	1.24	1.39	1.50	1.72
$\rho \times 10^3$, kg/m^3	1.43	1.43	1.43	1.43	1.43	1.43
$\lambda \times 10^{-1}$, w/m · K	3.69	3.86	4.05	4.04	4.03	4.30
$\alpha \times 10^{-7}$, m^2/s	2.6	2.5	2.2	2.0	1.9	1.8

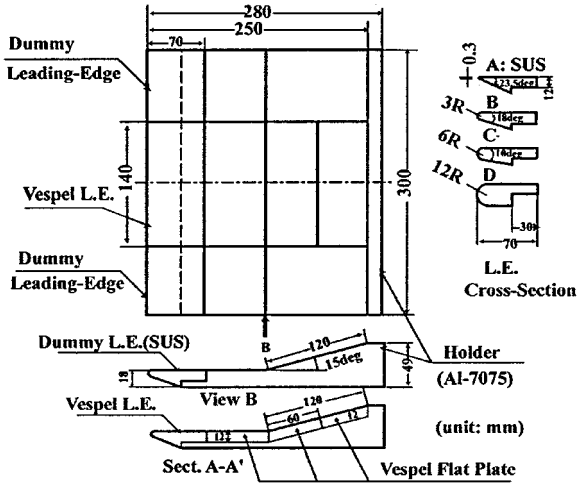

Fig. 1 Geometry of the models.

The model aspect ratio should be AR = 1 to satisfy the limit that can provide two dimensionality in a compression ramp region[8] and minimize three-dimensional effects on the measured heat fluxes. The ramp was made long enough so that the flow near the trailing edge gives little influence on the interacting corner flow, and yet the model size will not exceed the maximum permissible blockage of the tunnel. As a result, AR = 1.15 as the largest aspect ratio for a given configuration and for flow conditions was selected.

The manufactured finished model tolerance in the model scale is ±0.05 mm, and the model surfaces of the central plate was polished to 0.0063 mm in mean roughness height.

Instrumentation and Data Reduction

Apparatus and Instrumentation

To obtain a time history for the model surface temperature, the NAL and the ONERA IR imaging systems were used for each tunnels. The camera framing rates are 15 and 25 frames per second and the temperature resolutions are 12 bit for the NAL and the ONERA systems, respectively. The model's windward surface temperature images were observed through the Ge and ZnSe windows. Cameras were placed within an atmospheric pressure box in the test chamber of the tunnel and outside the test chamber in the NAL and the ONERA tests, respectively.

To avoid an initial heating disturbance from the shear layer around the mainstream, high-speed injection systems were used in both tunnels. The injection speeds were 0.18 and 0.20 s for the NAL and the ONERA tests, respectively. With use of these injection systems and proper determination of the starting time of assumed step heating, the measurement uncertainty caused by initial heat flux disturbance decreased less than 0.5% of the measured value.

Surface Heating Rate Reduction

The heat flux for each pixel of the image was extracted assuming one-dimensional conduction by modified Jones–Hunt methods (see Ref. 9) and the finite difference method[10] in the NAL and ONERA data reduction, respectively. Because Vespel has low thermal conductivity and thermal diffusivity properties, small lateral conduction effects were expected in the tests. Therefore, the reduction methods were adequate except for certain local, extremely severe peak heating regions.

The use of accurate thermophysical properties is necessary for the proper quantitative extraction of heat flux. The temperature-dependent material properties were used in ONERA data reduction. Constant thermal physical properties at 50°C were used for the NAL data reduction. In the case of the constant thermal properties, because of the relatively large temperature dependency of Vespel's thermal properties and the large temperature increase in the reattachment point heating region, it was necessary to study the temperature dependency effect of thermal properties on the reduced heating rate.

To find suitable constant thermal properties and to examine the accuracy of the measured IR heat-flux data, heat-flux measurements were simultaneously made by reference sensors (3 Gardon gauges and 3 slug calorimeters) at 6 points on the model in the previous NAL tests.[4] The difference of the amount of heat flux measured by IR thermography and the reference sensors was less than 3% of the measurement value by IR thermography. The sensors should be carefully installed on the model to eliminate heat conduction to the sensor from the surrounding hotter Vespel plate. The factors that determine the measured data accuracy in IR thermography are discussed in Ref. 9.

Flowfield Observation

The flowfield observation, by means of a schlieren system, was implemented at the NAL 1.27-m hypersonic wind tunnel to visualize the interacting flow structure.

Oil-flow observation was also conducted to obtain surface-flow information on the model surface. The mixture used for the observation was composed of different viscosity silicon-oils and TiO_2. The added TiO_2 increases the contrast with respect to the black surface of the model. To observe the development of shear stress lines on the surface of the model during the experiments, a charge-coupled device camera was installed in the plenum chamber of the wind tunnel and photographs were taken during the run to avoid oil-flow pattern changes by interference with the terminating shock.

Computational Fluid Dynamics Comparison Studies

In Ref. 4, studies between the experimental and computed heat-flux data showed insufficient agreement for cases with high angles of attack. Two possible reasons arise for this discrepancy. One reason is that the reattaching flow was transitional because of the high pressure and heat flux at the reattaching region on the ramp. The other possibility is that there may exist a three-dimensional effect for cases with high angles of attack.

In the present study, to further examine these possibilities, two kinds of computations were performed, one with the ONERA CELHYO2D code and the other with the three-dimensional NAL HYPER3D code, which solves laminar and turbulent Navier–Stokes equations, assuming perfect-gas conditions.

Code Description

The ONERA computation was performed with CELHYO2D, which solves laminar/turbulent Navier–Stokes equations assuming perfect or nonequilibrium air. CELHYO2D is a two-dimensional or axisymmetric Navier–Stokes code. The CELHYO solver deals with ideal mixtures of perfect gases. For thermochemical nonequilibrium flows, it usually assumes five neutral species. The chemical reaction model used for air is that of Gardiner.[11] It consists of 15 dissociation and 2 exchange reactions. Vibrational relaxation of the diatomic species occurs through vibrational–translational transfers, which are modeled following Landau–Teller's rule. The mixture viscosity is calculated after Sutton's model. In this study, a perfect-gas version was used. The CELHYO code solves the Navier–Stokes balance equations taking physical modeling on curvilinear structured meshes into account by using a fully implicit finite volume method. The viscous part is discretized according to a central-differencing procedure, whereas a quasi-second-order accurate upwind scheme yields an approximation for the inviscid operator. Upstreaming is achieved using the hybrid upwind splitting for upwind bias. Second-order accuracy was achieved by using a MUSCL approach that was written in primitive variables.

The computational mesh is composed of three blocks that are each (70×80) with a refinement near the wall to capture the boundary layer.[4] More detailed description of the code may be found in Refs. 12 and 13.

For the NAL three-dimensional computation, a flux-split upwind total variation diminishing thin-layer Navier–Stokes computational fluid dynamics (CFD) code, HYPER 3D,[14] was used. Computations using this code were primarily performed for the model B and D configuration at angles of attack from 0 to 30 deg. The computational mesh consists of 201 points in the streamwise and 101 points in the body-normal direction. Grids were generated using hyperbolic partial differential equations, and grid lines intersected at almost right angles on the flat plate surface. These good grid characteristics were very important in obtaining accurate heat transfer distributions.

Results and Discussion

Tunnel-to-Tunnel Comparison of Test Results

To evaluate appropriately the measured heat transfer data, other reliable data or good analytical methods that can validate the magnitude of the measured data are necessary. The comparison of the present NAL/ONERA heat-flux measurements show quite good quantitative agreement for heat-flux distribution, as shown Fig. 2. The small difference of both data shows a high reliability of the obtained data. These data provide a good database for CFD code validation and for the numerical rebuilding of the flow structure around the compression corner with complicated multiple shock/shock interactions.

Heat Transfer Distribution

Figures 3 and 4 show examples of heat transfer distribution along the model centerline. At $\alpha = 35$ deg, large peak heating on the ramp was observed. The magnitude of peak heating decreases, and the location of the peak moves downstream with an increase in nose bluntness. At $\alpha = 30$ deg, expected heat transfer distributions on the ramp, as is commonly observed in reattaching flow, was observed, that is, peak heating downstream of the reattachment point followed by a gradual decrease of heat flux. At $\alpha = 15$ deg, a monotonic increase in heat flux on the ramp was observed. These aerodynamic heating characteristics were strongly connected to a type of triple bow/separation and corner shock interaction, as discussed in the next section.

Interacting Flow Structure Examination

To examine the relationship between the measured heating characteristics and the interacting flow, a flowfield analysis was performed by comparing the schlieren images.

$\alpha = 35$ Degree Case

For model A with a sharp leading edge, a clear schlieren observation is obtained (Fig. 5), because there are small entropy-layer effects on the shock-layer density distribution. Figure 6 shows the estimated flowfield from the schlieren observation for model A at $\alpha = 35$ deg. By the use of a shock polar analysis (Fig. 7) assuming recirculating separated flow as a wedge with an effective angle of flow deflection, approximately 4 deg, from the separation shock angle in the schlieren images for a flat plate flow of $M_1 = 2.16$, a detail of the flowfield (Fig. 8) was accurately rebuilt.

Flow region 4 behind the nose/separation shock interaction point P is the subsonic region and regions 4 and 3 are separated by a slip surface. There is also a weak slip surface between regions 5 and 6 behind intersection T of the shock PT and the corner shock BT. The induced shock TR reached the ramp surface and induced peak heating. This interaction seems to be close to the Edney type V,[15] but there is no supersonic jet flow behind the point P.

The TR shock may possibly create a Mach reflection, when the Mach number and shock angle, $M = 1.61$ and $\theta = 47.2$ deg, in flow region 6 are considered. The peak heating location seems to agree with the shock TR impingement location.

Supplemental oil-flow observations were also conducted to examine the interacting flow structure. Based on the surface oil-flow observation in Fig. 9, one can illustrate the estimated surface flow topology, as shown in Fig. 10, which is consistent with the interacting flow structure of Fig. 8. Two induced separation lines, S2 and S3 (before and after the primary shear-layer reattachment line R1), are clearly detectable from the oil-flow image. The impinging shock TR may cause the separation S3 and the reattachment R3. The oil-flow image shows a secondary separation line S2 within the corner separation region indicating a further flow recirculation. Basic topological rules[16] demand the corresponding reattachment, R2 but this reattachment line is not visible in the oil-flow pattern.

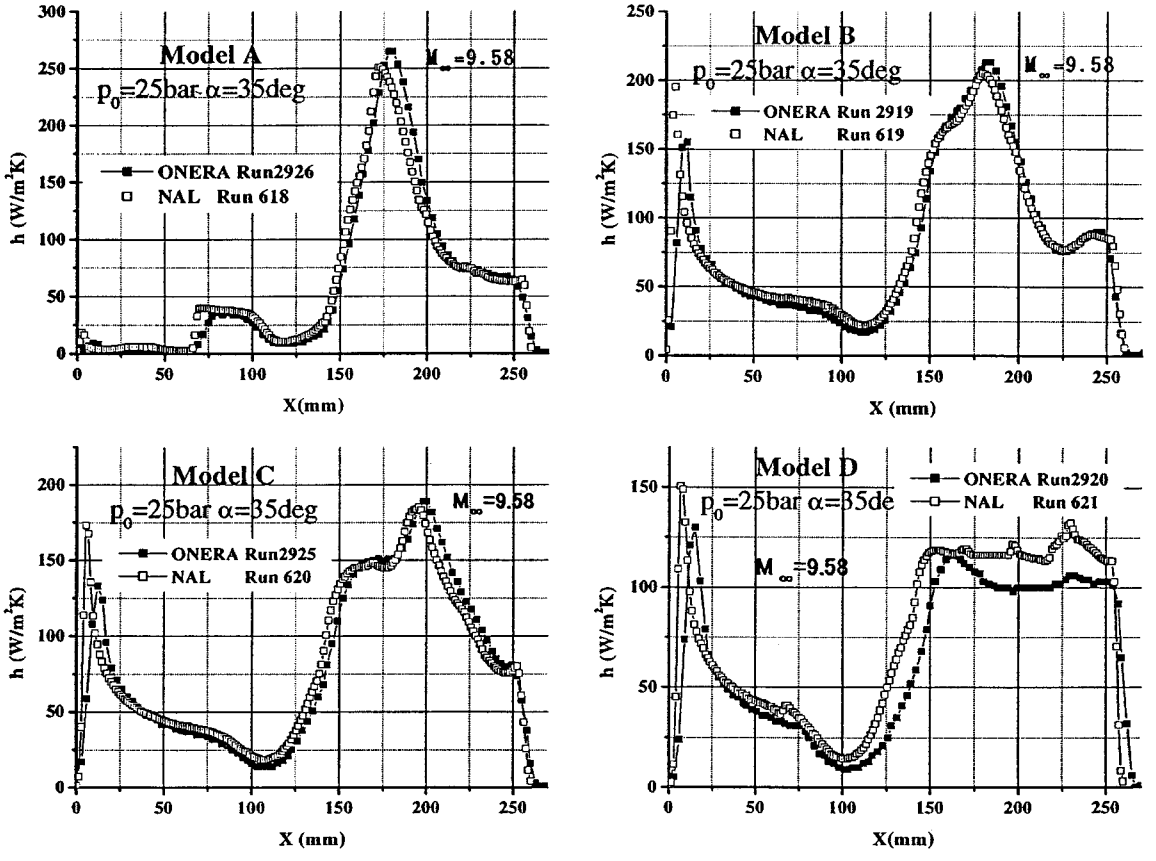

Fig. 2a NAL/ONERA heat transfer data comparison; α =35 deg.

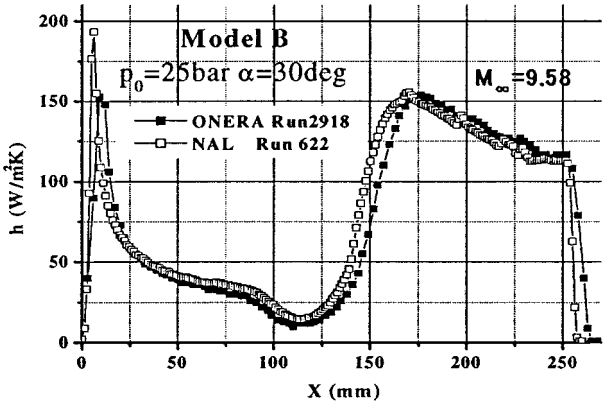

Fig. 2b NAL/ONERA heat transfer data comparison; α = 30 deg.

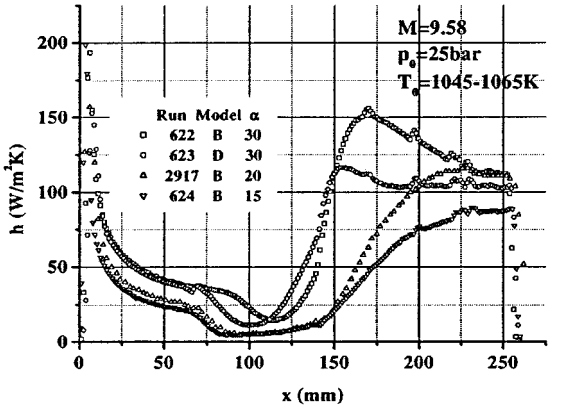

Fig. 4 Centerline heat transfer distribution; p_0 =25 bar and α = 30, 20, and 15 deg.

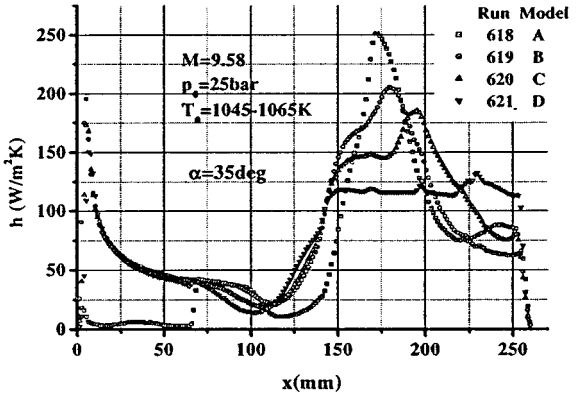

Fig. 3 Centerline heat transfer distribution; p_0 = 25 bar and α = 35 deg.

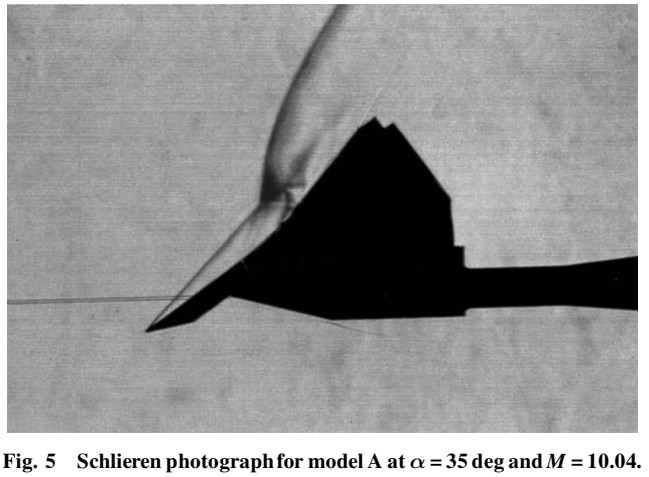

Fig. 5 Schlieren photograph for model A at α = 35 deg and M = 10.04.

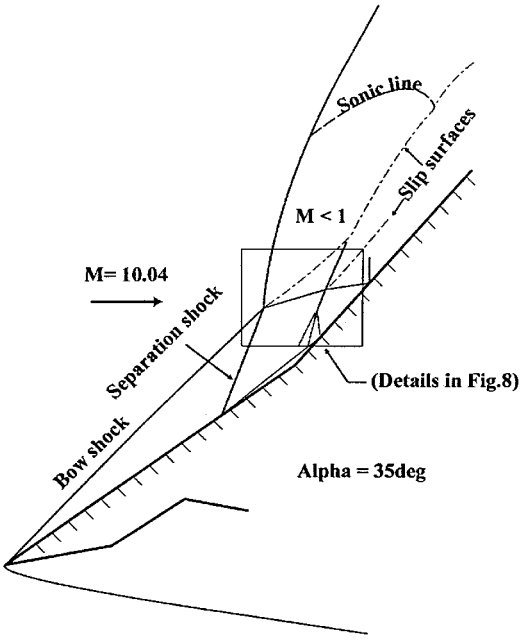

Fig. 6 Flowfield estimated from schlieren observation: model A, p_0 = 25 bar, and α = 35 deg.

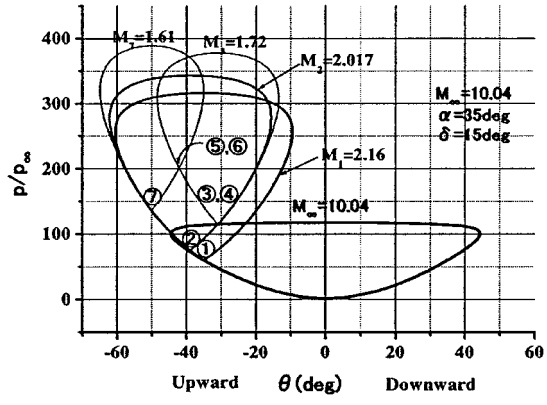

Fig. 7 Shock polar diagram for sharp leading-edge model: model A, p_0 = 25 bar, and α = 35 deg.

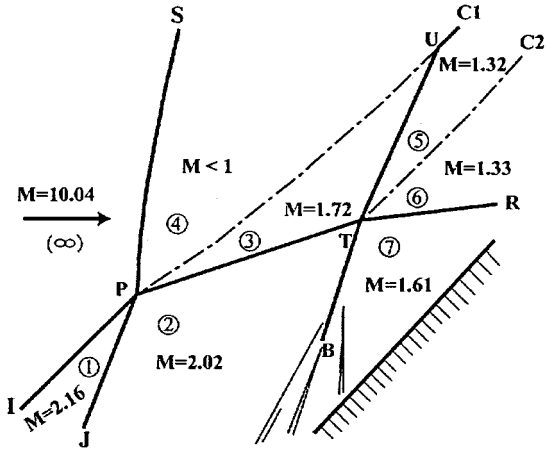

Fig. 8 Detail of the flow structure for schlieren observation.

$\alpha = 30$ Degree Case

The inviscid shock polar diagram for sharp model A at $\alpha = 30$ deg shows that almost the same type of interaction as in $\alpha = 35$ deg case will occur (Fig. 11). As shown in Fig. 4, with decreasing α the magnitude of the peak heating decreases, and the heating pattern changes as compared with the $\alpha = 35$ deg case seen in Fig. 3. For model B, the shock shape, after the interaction point P also shows that the type of interaction and the flow structure may be the same

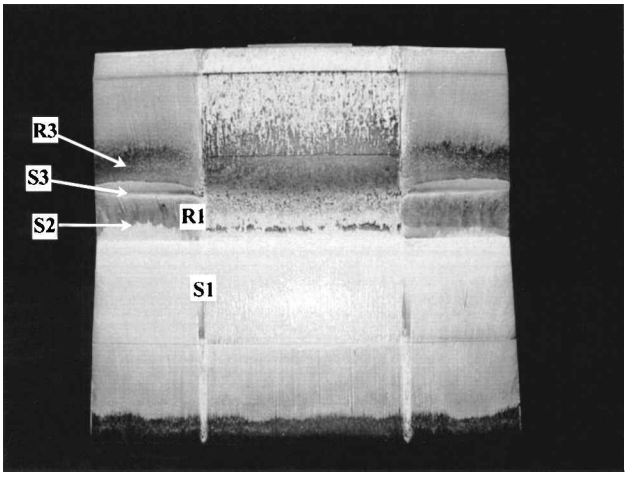

Fig. 9 Surface oil-flow pattern: model A, p_0 = 25 bar, and α = 35 deg.

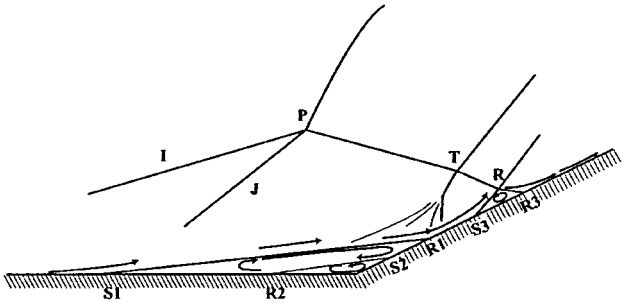

Fig. 10 Estimated separated flowfield for model A at α = 35 deg.

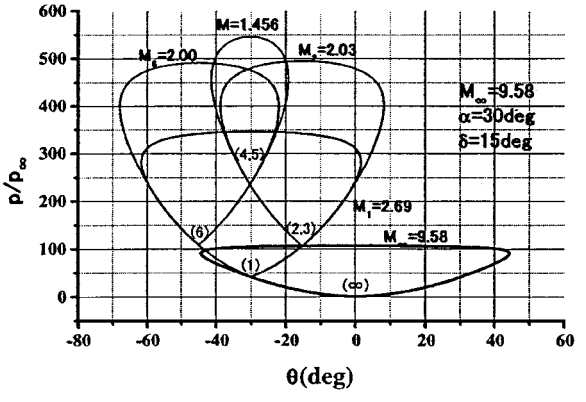

Fig. 11 Inviscid shock polar diagram for a model with sharp leading edge at α = 30 deg.

as in the $\alpha = 35$ deg case (Fig. 12). Although it is not clear whether the shock TR impinges the ramp wall or not from Figs. 4 and 12, the shock TR impinging point may be far from the hinge line, which can be expected from the downstream movement of the interaction point P, as seen in Fig. 12 and in the peak heating location of the model A case (run 341) in Fig. 13.

For model D (run 623), the shock wave angle at the interaction point P shows that there is no subsonic region. Flow region 7 occupies almost all parts of the ramp, and the development of the boundary layer, after the reattachment in flow region 7 may determine the peak heating position and heat-flux decrease downstream.

$\alpha = 15$ Degree Case

Figure 14 shows the estimated shock polar diagram for the interacting flow around the model B at $\alpha = 15$ deg. Figure 15 shows the schlieren observation of the additional tests of model B at $\alpha = 15$ deg. The corresponding flow structure for model B estimated from Figs. 14 and 15 is shown in Fig. 16.

Bow/separation shock interaction occurred fairly forward on the upstream side, and there is no more subsonic region behind the

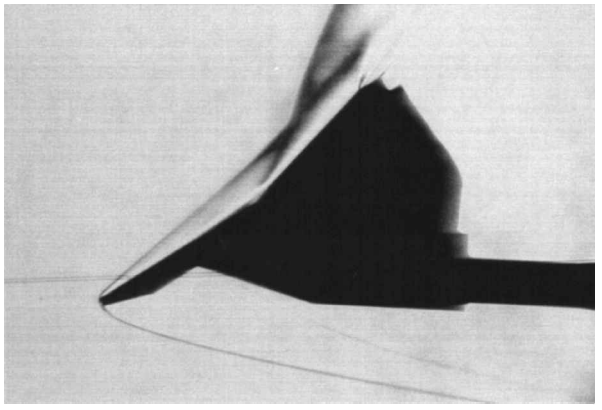

Fig. 12 Schlieren photograph for model B: p_0 = 25 bar, α = 30 deg, and M = 9.58.

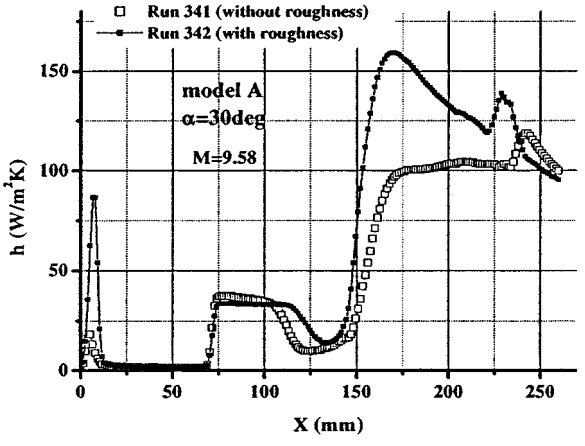

Fig. 13 Centerline heat transfer distribution: model A, p_0 = 25 bar, and α = 30 deg.

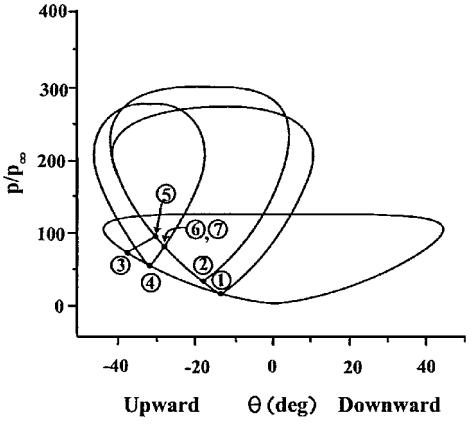

Fig. 14 Shock polar diagram for model B at p_0 = 25 bar and α = 15 deg.

interaction point. The expansion fan from the bow-shock/separation-shock interaction point is reflected by the compression corner shock and does not reach the ramp. Therefore, the heat transfer distribution on the ramp increased monotonically without a heat-flux distribution dent induced by the expansion fan impingement on the ramp (which occurs in an Edney type VI interaction[15] for two-shock-interaction cases).

From the preceding examination, it became clear that for the compression corner flow of sharp-nosed flat plates with triple-shock interaction, separation shock plays the most important role with a combination of the extent of the separation region to determine the ramp heating characteristics.

The angle-of-attack effect and the nose-bluntness effect on the ramp heating characteristics is evident from the present experimental data. The influence of the leading-edge bluntness on the separation length may be important because it determines the streamwise heat transfer over the flap. The (laminar) separation point before the hinge line moves strongly upstream when the leading edge is rounded for high angles of attack. This behavior should be carefully examined by evaluating the three-dimensional effects, as will be discussed later.

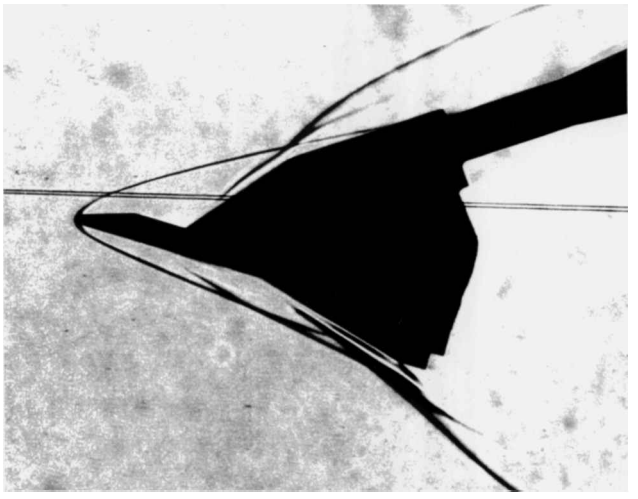

Fig. 15 Schlieren photograph for model B: p_0 = 25 bar, α = 15 deg, and M = 9.58.

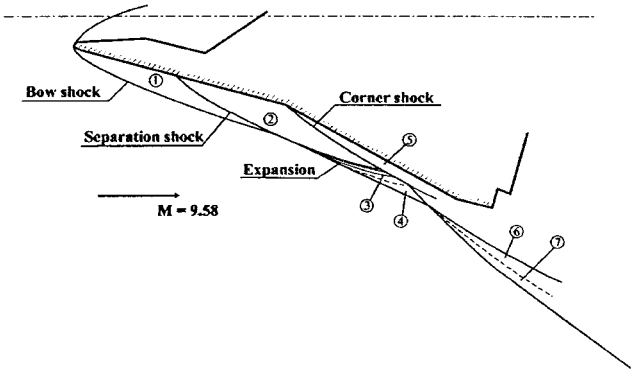

Fig. 16 Detail of the flowfield from the schlieren observation: model B, p_0 = 25 bar, and α = 15 deg.

Two-Dimensional Computational Study

The computations were performed to rebuild the experimental results of S4MA runs number 2917, 2918, and 2923.

Laminar Flow Calculation

Laminar computations were first performed. The computed iso-Mach lines are shown for run 2917 and 2918 test conditions in Fig. 17. The computed heat transfer coefficient is compared with the experimental data in Fig. 18.

Strong differences appear in the level of heat transfer coefficient on the ramp and also in the length of the separated region. This length was much greater in the calculations, but this result was not the case for the 0-deg angle of attack in the model B cases.[4]

The bidimensional flowfield behavior, that is, heating pattern change during a run, was verified using IR views during the run. To explain such a difference, it was agreed to perform turbulent computations.

Turbulent Flow Calculation

The turbulent computations were performed using the Baldwin–Lomax turbulence model. The present analysis of the transition-onset point adjustment showed very close shock shape between the CFD results and the schlieren observation.

The dashed line in Fig. 19 shows an example of the two-dimensional turbulent calculation. In this case, the distribution

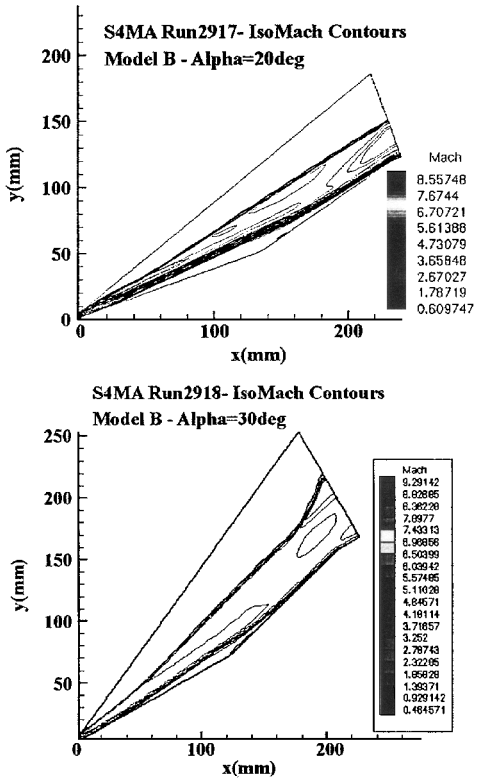

Fig. 17 Iso-Machcontours for runs 2917 and 2918.

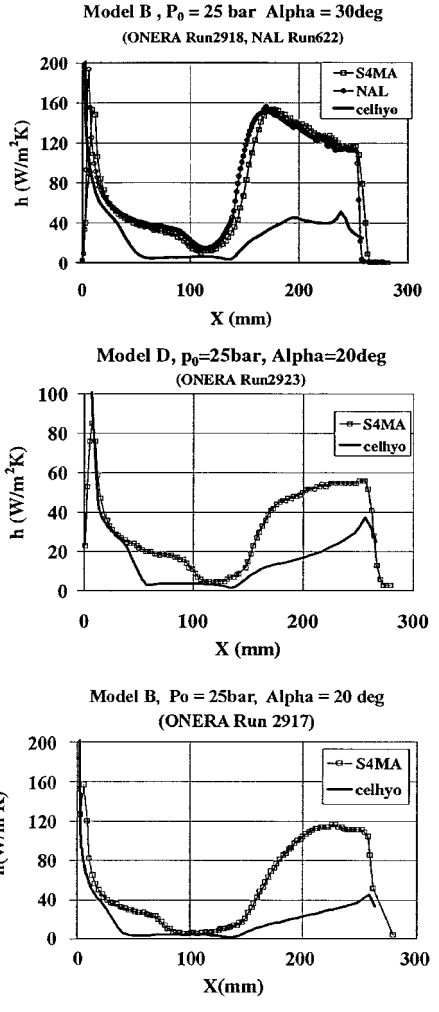

Fig. 18 Comparison of experimental results with laminar two-dimensional calculation.

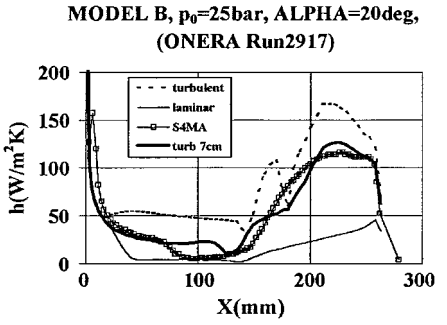

Fig. 19 Example of turbulent two-dimensional calculation.

seems to exhibit the start of a plateaulike region ahead of the ramp, which looks like it is showing characteristics of a turbulent interaction, but the heat transfer distribution on the ramp did not show good enough agreement with the test results.

The bold solid line shows an example of a calculation in the transition-onset point adjustment analysis assuming that flow becomes turbulent at the flow separation region (at $x = 70$ mm from the leading edge). This calculation result showed best agreement with the S4MA test data as compared with fully laminar and turbulent results. This result may show that the flow is transitional although the calculated separation region size was smaller.

Examination for the Occurrence of Transition

From the described results, the following two questions arose: 1) whether transition of the separated shear layer and the reattaching boundary layer actually occurred in the present tests within the interaction process and 2) whether a two-dimensional calculation is sufficient to compare to the experiment.

To obtain insight into solving these two queries, the results of two short tests (i.e., previous roughness tests and additional oil-flow observation tests in the NAL hypersonic tunnel) were examined.

Roughness Test Results

To confirm heat flux distribution on the ramp for the transitional cases, roughness tests were performed by installing a carborundum band, with an average roughness height of 0.3 mm, at $x = 2r_n$ ($x = 1$ mm for model A) distance from the leading edge. Figures 13 and 20 show the heat transfer distribution comparison between the tests with and without a roughness trip for model A. (Because a stainless steel leading edge was used for model A to avoid the model leading-edge contamination for the small nose bluntness model, data $x < 70$ mm should not be used as the heat transfer data.)

On the flat plate, although there is a small difference shown for the magnitude of heat flux caused by a difference in the entropy-layer swallowing effect, the heating profile and the separation point is almost the same, showing that the flow stays laminar on the flat plate. On the ramp, there is a clear difference that shows a large heating peak for roughness test cases.

For run 346, a well-developed strain heating pattern was observed in the region between the area downstream of the reattachment and upstream of the peak heating line, indicating that an increase in heating by Görtler vortices occurs.[17] This result reveals that a concave shear-layer surface exists between separated flow reattachment and the TR shock impingement line, which may be caused by the occurrence of transition in the separated shear layer.

Roughness tests for model D at $p_0 = 25$ bar and $\alpha = 20$ deg were also conducted. Exactly the same centerline heat transfer distribution as the case without roughness was obtained. This result provided no definite evidence on the occurrence of transition for large bluntness models, indicating the following two possibilities: 1) flow remained laminar because of a slight sensitivity to roughness or 2) flow was already turbulent. To judge which is correct, one must depend on the CFD results described in the preceding sections.

The most important observation, shown in Figs. 13 and 20, is that the separation length from the ramp corner plays a significant role in determining the heat transfer distribution on the ramp. Figure 13 shows a decrease in the separation region in the roughness

test (run 342). This decrease of the separation length changes the interaction flow structure by changing the location of the bow and separation shock intersection point P and the resulting shock shape. The difference in heat transfer distribution on the ramp may arise from this difference in the flow structure, although there may be a difference in heating levels from the laminar-flow case of run 341.

Figure 20 shows almost the same separation length and a similar heat transfer distribution on the ramp in runs 337 and 346. This similarity seems to come from that the same separation length induces the same inviscid interacting flow region and produced a similar heat transfer distribution on the ramp. The higher heating level in run 346 definitely comes from that the flow is turbulent on the ramp in the roughness test of run 346 although there may be some amount of heating increase by Görtler vortices.

Oil-Flow Observation Results

To confirm the amount of flow three dimensionality in the present tests, additional tests for surface oil-flow observation were conducted. The results of the oil-flow observation shows that the three dimensionality of the flow is large for the large nose bluntness case (model D) at $\alpha = 0$ and 35 deg.

Figure 21 shows the outer surface flow and the singular point (nodal point) on the model holder surface. Figure 9 shows that there is a smaller outer flow for the small nose bluntness case of model A. This observation on the influence of nose bluntness is the same as the shock/boundary interaction experiment in Ref. 18 for zero-angle-of-attack cases. The investigations of Ref. 18 attributed the reason for these experimental results to the pressure balance relating to the high-pressure region generated by the leading-edge shock.

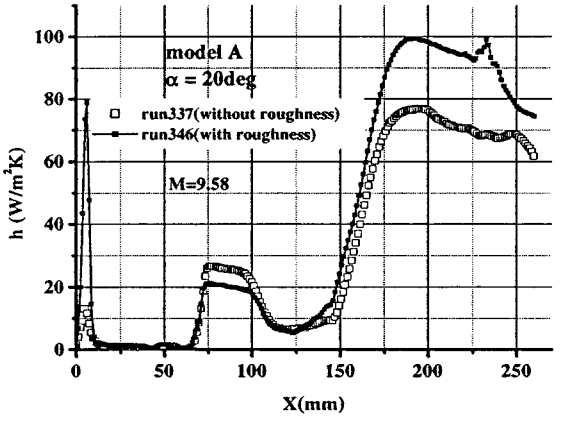

Fig. 20 Comparison of roughness effect on centerline heat transfer distribution: model A, p_0 = 25 bar, and α = 20 deg.

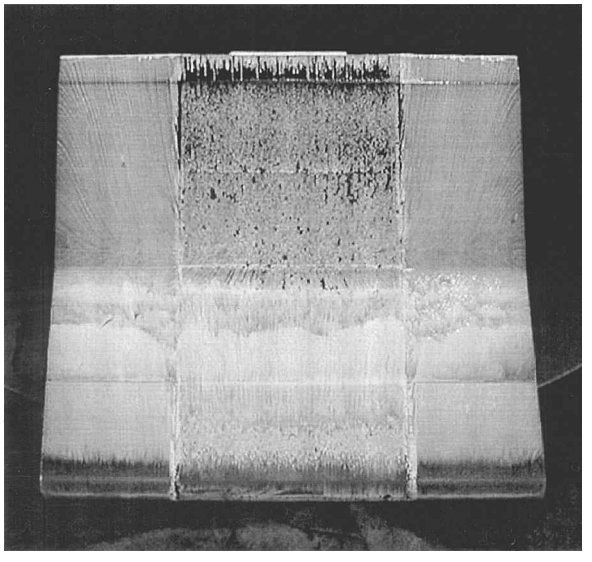

Fig. 21 Surface oil-flow pattern: model D, p_0 = 25 bar, and α = 35 deg.

These experimental facts may explain one reason for the discrepancy between the two-dimensional calculation and the experimental results and demonstrate the necessity of evaluation of the true three-dimensional effects by comparing them with both two- and three-dimensional calculation results.

Comparison with Three-Dimensional Numerical Simulation

Figure 22 shows an example of shock shape comparisons for model D at $\alpha = 20$ deg. Figure 22a is a comparison between two-dimensional computational results and the corresponding schlieren photograph. The white line contours shown are computed iso-Mach lines. A large discrepancy was observed in the shock shape at the lower compression ramp side, whereas the three-dimensional computational results in Fig. 22b show good agreement with the NAL1.27 m wind-tunnel experiments. Similar results are shown for the $\alpha = 30$ deg condition of the same model.

NAL M10 tunnel data were compiled for model B at $\alpha = 0$ in Fig. 23. Two-dimensional CFD results show a large separation region at the junction of the flat plate and the compression ramp. On the other hand, three-dimensional calculation can predict heat transfer distributions more accurately. In general, it may be concluded that the three dimensionality of flow characteristics cannot be disregarded, even for cases of low angles of attack.

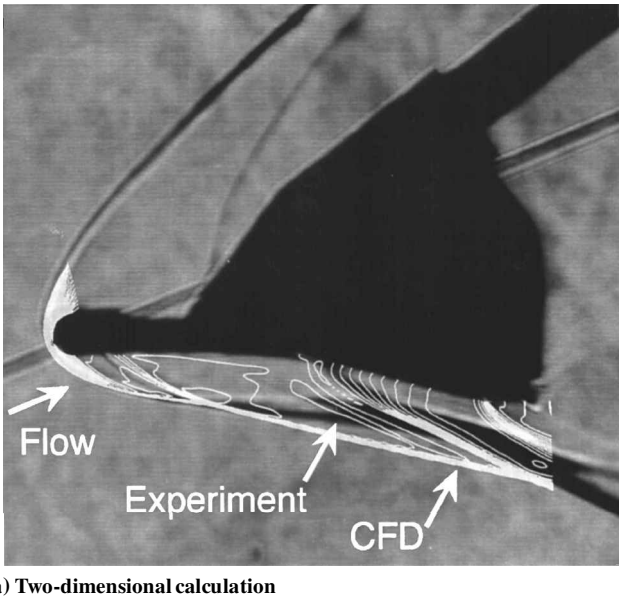

a) Two-dimensional calculation

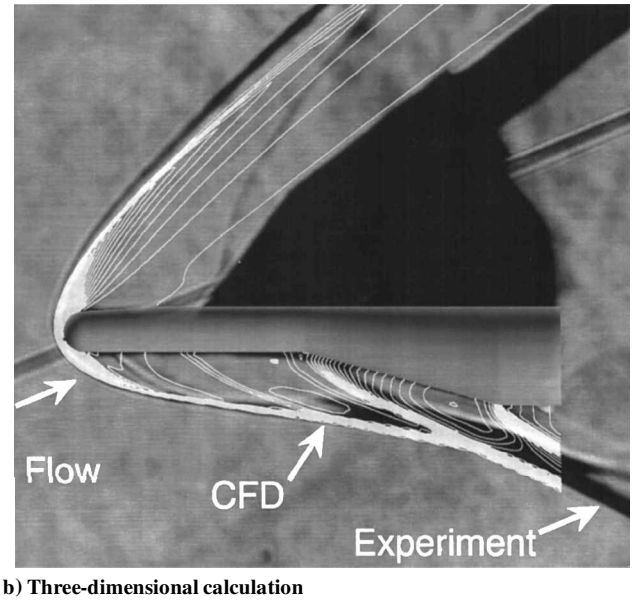

b) Three-dimensional calculation

Fig. 22 Comparison of shock wave geometry: model D, M = 10.04, p_0 = 25 bar, and α = 20 deg.

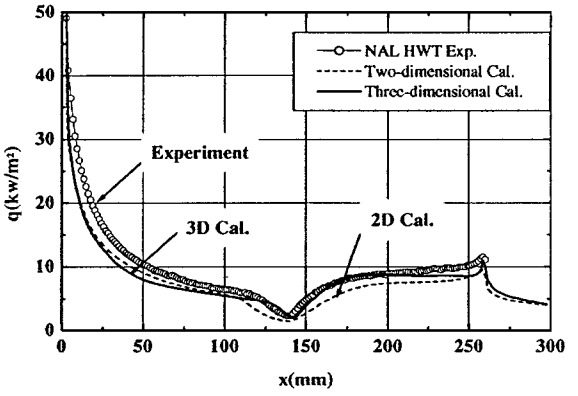

Fig. 23 Two- and three-dimensional heat transfer distribution comparison: model D, $M = 10.04$, $p_0 = 25$ bar, and $\alpha = 0$ deg.

As already discussed, for accurate numerical rebuilding of the present experimental results, it is necessary to reproduce the flow structure of complex multiple shock interactions with separation. The reproduction of the separation length, an effective amount of separated flow disturbance (separation shock angle), and the resulting position of shock interaction point P (shock geometry) are important because they provide the resulting influence on ramp heating.

The effect of flow transition and three dimensionality are also important because they provide large influences on the interacting flow structure. From the present experimental data, no definite conclusion could be drawn concerning whether the interacting flow is laminar or not in the flow regions after reattachment.

However, the two-dimensional transitional calculations for models B and D indicated a high possibility of turbulent flow on the ramp. For the three-dimensional calculation in Fig. 23, the heating level was lower than the experimental value at $x < 140$ mm, although the calculated shock shape and separation length are almost same as the experimental ones. Consistency of the heat-flux increase on the flat plate, which may be induced by small leading-edge bluntness, was examined by a correlation study of the heat transfer distribution in Ref. 4. The numerical rebuilding of this heat flux increase is a subject for study in the future.

Conclusions

By the use of the experimental heat transfer data for a blunt-nosed flat plate model with a 15-deg compression ramp, the relationship between the heat transfer distribution and the interacting flow around the ramp, with variable angles of attack and nose bluntness, were examined. The following results were obtained in the present study.

At a high angle of attack, bow/separation shock and corner shock interactions were very close to the Edney type I, V, and VI interactions, but with some notable differences.

These interactions provided a dominant influence on the ramp heat-flux distribution and the amount of peak heating. Separation length, which is determined by a combination of angle of attack, leading-edge bluntness, and the position of the bow/corner shock interaction point, play an important role in determining the heat-flux distribution on the ramp.

It will be necessary to evaluate the three-dimensional effects on the interacting flow structure and to clarify the mechanism of the onset of transition in the flow for accurate empirical and numerical rebuilding of the heating characteristics around the compression ramp.

Acknowledgments

Support in part by the international cooperation program of Science and Technology Agency in Japan is gratefully acknowledged. This study was performed based on mainly the second testing campaign within the framework of the ONERA/NAL cooperation agreement signed in February 1995. The authors would like to gratefully acknowledge X. Bouis of the ONERA Computing, Engineering and Testing Facilities for his help and support during the present cooperation and all who participated in conducting the cooperation tests in the NAL 1.27-m and ONERA S4MA hypersonic wind tunnels.

References

[1]Holden, M., "Experimental Studies in Shock Wave Boundary Layer Interactions," AG-203, AGARD, June 1975.

[2]Delery, J. M., and Marvin, J. G., "Shock-Boundary Layer Interactions," AG-280, AGARD, Oct. 1986.

[3]Holden, M. S., "A Study of Flow Separation in Regions of Shock-Wave/Boundary-Layer Interaction in Hypersonic Flow," AIAA Paper 78-1169, July 1978.

[4]Hozumi, K., Yamamoto, Y., Fujii, K., Yoshizawa, A., Nagai, S., Devezeaux, D., and Fontaine, J., "Experimental Investigation and Numerical Analysis of Hypersonic Compression Ramp Heat Transfer," *Japan Society of Mechanical Engineers International Journal, Series B*, Vol. 41, No. 2, 1998, pp. 381–389.

[5]Olejniczak, J., Candler, G. V., and Wright, M. J., and Leyve, I., and Hornung, H. G., "Experimental and Computational Study of High Enthalpy Double-Wedge Flows," *Journal of Thermophysics and Heat Transfer*, Vol. 13, No. 4, 1999, pp. 431–440.

[6]Olejniczak, J., Wright, M. J., and Candler, G. V., "Numerical Study of Inviscid Shock Interactions on Double-Wedge Geometries," *Journal of Fluid Mechanics*, Vol. 352 , 10 Dec. 1997, pp. 1–25.

[7]Nomura, S., Sakakibara, S., Hozumi, K., and Soga, K., "NAL New Hypersonic Wind Tunnel Systems," AIAA Paper 93-5006, Nov. 1993.

[8]Lewis, J. E., Kubota, T., and Lees, L., "Experimental Investigation of Supersonic Laminar, Two-Dimensional Boundary-Layer Separation in a Compression Corner with and Without Cooling," *AIAA Journal*, Vol. 6, No. 1, 1968, pp. 7–14.

[9]Hozumi, K., Nagai, S., Fujii, K., Yoshizawa, A., and Hara, N., "Effect of Slight Leading Edge Bluntness on Flat Plate Heat Transfer and Boundary Layer Transition at Hypersonic Mach Numbers," *Proceedings of the 19th Congress of the International Council of the Aeronautical Sciences*, AIAA, Washington, DC, 1994, pp. 1220–1230.

[10]Consigny, H., Sant, Y., Le Bouvier, F., Baumann, P., and Merienne, M. C., "Heat Transfer Measurement Techniques Used or in Development at ONERA/Chalis-Meudon," *New Trends in Instrumentation for Hypersonic Research*, NATO ASI Series, Ser. E: Applied Sciences, Vol. 224, Kluwer Academic, Norwell, MA, 1994, pp. 437–447.

[11]Gardiner, W. C., Jr., *Combustion Chemistry*, Springer-Verlag, New York, 1984, pp. 1–19.

[12]Sagnier, P., and Verant, J. L., "Flow Characterization in the ONERA F4 High-Enthalpy Wind Tunnel," *AIAA Journal*, Vol. 36, No. 4, 1998. pp. 522–531.

[13]Coquel, F., and Marmignon, C., "Roe Type Linearization for the Euler Equations for Weakly Ionized Multi-Component and Multi-Temperatures Gas," AIAA Paper 95-1675, June 1995.

[14]Yamamoto, Y., "Numerical Simulation of Hypersonic Viscous Flow for the Design of H-II Orbiting Plane (HOPE); Part II," AIAA Paper 91-1390, June 1991.

[15]Edney, B., "Anomalous Heat Transfer and Pressure Distributions on Blunt Bodies at Hypersonic Speeds in the Presence of an Impinging Shock," Aeronautical Research Inst. of Sweden, FFA Rept. 115, Stockholm, Feb. 1968.

[16]Peak, D. J., and Tobak, M., "Three-Dimensional Interactions and Vertical Flows with Emphasis on High Speeds," AG-252, AGARD, July 1980.

[17]Domröse, U., Krause, E., and Meike, M., "Numerical Simulation of Laminar Hypersonic Shock-boundary Layer Interaction," *Zeitschrift für Flugwissenschaften Weltraumforsch*, Vol. 20, No. 2, 1996, pp. 89–94.

[18]Kreins, A. F., Henckels, A., and Maurer, F., "Experimental Studies of Hypersonic Shock Induced Boundary Layer Separation," *Zeitschrift für Flugwissenschaften Weltraumforsch*, Vol. 20, No. 2, 1996, pp. 80–88.

M. Torres
Associate Editor